Diverse binding poses of agonistic neurotoxins on human $Na_v1.6$

Xiao Fan[1,5], Jian Huang[1,5,7], Lin Yang[2,5], Jiaofeng Chen[2,6], Huan Wang[2,6], Xiaoshuang Huang[1], Jinli Geng[2], Qinglin Wu[2], Yuzhen Xie[1], Fangzhou Lu[1,4], Qinmeng Guo[2], Zilin Shen[1], Xueqin Jin[2,7], and Nieng Yan[1,2,3,7]

[1]Institute of Bio-Architecture and Bio-Interactions (IBABI), Shenzhen Medical Academy of Research and Translation, Guangming District, Shenzhen 518107, Guangdong, China

[2]Beijing Frontier Research Center for Biological Structures, State Key Laboratory of Membrane Biology, Tsinghua-Peking Joint Center for Life Sciences, School of Life Sciences, Tsinghua University, Beijing 100084, China

[3]Institute of Chemical Biology, Shenzhen Bay Laboratory, Guangming District, Shenzhen 518132, Guangdong, China

[4]Westlake University, Hangzhou 310024, Zhejiang, China.

[5]These authors contribute equally. [6]These authors contribute equally.

[7]To whom correspondence should be addressed: Nieng Yan (nyan@tsinghua.edu.cn); Jian Huang (huangjian@smart.org.cn); Xueqin Jin (jinxq@mail.tsinghua.edu.cn).

Abstract

Na_v channels are key targets for various venomous toxins. Deciphering their binding poses and mechanisms of action (MOAs) will facilitate therapeutic development targeting Na_v channels. Here we present distinct binding poses of three agonistic peptide toxins on human $Na_v1.6$ through high-resolution cryo-EM structures. The globular β-scorpion toxin Cn2 nestles between the extracellular segment of VSD_{II} and the pore extracellular loops in the third repeat (ECL_{III}), where it is stabilized by interactions with both protein regions and the branched N1372-glycan. ι-Conotoxin RXIA adopts an elongated conformation, spanning VSD_I and VSD_{IV} to wrap around the shoulder of the pore domain (PD). The bullet ant-derived toxin Pc1a (poneratoxin) exists as a transmembrane helix that inserts between VSD_{II} and PD_{III}. Our findings, corroborated by functional characterizations, illustrate the remarkable diversity in peptide toxin binding modes and MOAs, providing a foundation for the rational design of selective Na_v channel modulators.

Introduction

Venomous organisms, such as snakes, spiders, scorpions, ants, and numerous marine species, secrete toxins for predation or defense [1]. Many of these toxins, either small molecules or peptides, target voltage-gated sodium (Na_v) channels, which govern membrane excitability in neurons and muscles [2-4]. These toxins can modulate channel activity by binding to specific sites and stabilizing particular working states, thus functioning as agonists or antagonists. They have proved valuable in characterizing Na_v channels and served as templates or leads for designing novel therapeutic agents [5-9]. Structural studies of channel-toxin complexes have afforded critical insights into their mechanisms of action (MOAs) and revealed the versatile receptor sites on Na_v, setting the framework for rational drug development [2,10].

Recently, we investigated the modulation of $Na_v1.6$ by an antagonistic peptide toxin PaurTx3 and revealed three binding poses of the toxin [11]. $Na_v1.6$, encoded by *SCN8A*, is widely expressed in both the central and peripheral nervous systems, with a high density at the distal axon initial segment and nodes of Ranvier, where it initiates action potentials (APs) [12-16]. As $Na_v1.6$ channels are present in both excitatory and inhibitory neurons, either loss-of-function (LOF) or gain-of-function (GOF) mutations can be associated with pathologic conditions [17-19]. LOF mutations in *SCN8A* have been characterized in patients with motor impairment and intellectual disability, and GOF mutations are associated with developmental and epileptic encephalopathy (DEE) [17,19-23].

Although both antagonists and agonists hold therapeutic promise, the latter has been

disproportionally underexplored. In fact, the majority of available mammalian Na_v-toxin structures concern inhibitors [2,10,24-30], with α-scorpion toxins (e.g., AaH2 and LqhIII) being the only agonists that have been structurally characterized to date [31,32]. As such, the MOAs of agonistic toxins remain largely unclear. In this study, we focus on the characterization of the MOAs of three agonistic gating modifier toxins (GMTs) on $Na_v1.6$, including the β-scorpion toxin Cn2, the ι-conotoxin RXIA (ι-RXIA) from fish-hunting cone snail, and the bullet ant-derived δ-paraponeritoxin-Pc1a (Pc1a) [33-37].

Cn2 has been proposed as a model drug to elicit deep brain stimulation for potential treatment of Parkinson's disease for its selectivity and dual modulatory effects, which are subject to the depolarizing conditioning pre-pulses [36]. Following a pre-pulse stimulus, Cn2 lowers the activation threshold and induces a transient resurgent current. Without pre-pulse, however, it blocks sodium current [36]. ι-RXIA similarly shifts the activation threshold to hyperpolarized voltages [34]. Its third-to-last residue is a D-Phe44, which has a substantially higher potency than the L-Phe44 counterpart, indicating a highly specific binding mode [38,39]. Pc1a is the main component in the venom of bullet ant *Paraponera clavata* [40]. It prevents the fast inactivation of Na_v channels, induces a sustained tail current, lowers activation voltage, and exhibits over 20-fold greater potency on $Na_v1.6$ than on other subtypes [40,41].

Here we present the high-resolution cryo-EM structures of human $Na_v1.6$ bound to each toxin, revealing three completely distinct binding poses. The structure-activity relationship studies reveal the molecular basis for their modulatory activities. Our systematic

characterizations highlight the versatile binding sites on Na_v channels for diverse modulators, and shed light on future therapeutic development.

Results

Cryo-EM analysis of $Na_v1.6$ with three toxins

We started by validating the activities of purchased and in-house synthesized toxins via whole-cell patch-clamp recording in HEK293T cells transiently expressing full-length human $Na_v1.6$. Cn2 indeed exhibits dual functionality. It blocks sodium current with an IC_{50} of 27.07 ± 3.15 nM without a pre-pulse, but shows agonistic activity after a + 40 mV pre-pulse, shifting the activation $V_{1/2}$ leftward by up to 35 mV and slowing fast inactivation from 0.37 ± 0.04 ms to 3.98 ± 0.66 ms (Figures 1A and S1A, Tables S1-S2). ι-RXIA markedly enhances the peak current in response to a V_{step} to -30 mV, with an EC_{50} of 0.69 ± 0.24 μM (Figures 1B and S1B). While primarily lowering the activation threshold, it also slightly slows fast inactivation and modestly shifts the inactivation $V_{1/2}$ to more hyperpolarized potentials (Figures 1B and S1B, Table S3). The synthesized Pc1a hyperpolarizes the activation curve by up to 50 mV, with an EC_{50} of 17.22 ± 1.06 nM (Figure 1C). The toxin drastically increases a persistent tail current, literally eliminating fast inactivation when applied at saturating concentrations, but meanwhile it prolongs the activation duration in the whole cell recording (Figure S1C and Tables S4-5).

To elucidate the molecular basis for their MOAs, we determined the cryo-EM structures of human $Na_v1.6$ in complex with each toxin following our established protocol [42]. High-resolution 3D EM reconstructions were obtained at 2.8 Å for $Na_v1.6$-Cn2, 2.5 Å for $Na_v1.6$-ι-

RXIA, and 3.1 Å for $Na_v1.6$-Pc1a (Figures 1D-F and S2, Table S6). Each toxin displays a unique binding pose, none of which has been previously observed.

Cn2 is grasped by VSD_{II}, ECL_{III} and a branched glycan

All 66 residues in Cn2 were unambiguously resolved to be accommodated on the extracellular side, between the voltage-sensing domain in repeat II (VSD_{II}) and the extracellular loop above the pore domain (PD) in repeat III (ECL_{III}), a site that is defined as V2EP [43]. The globular Cn2 toxin is clenched by the amino acid residues in VSD_{II}, ECL_{III}, and, importantly, a branched glycan chain linked to Asn1372 on ECL_{III} (Figures 2A and S3A).

Asn1372 is a conserved glycosylation site across human Na_v channels, but only the initial *N*-acetylglucosamine of the N1372-glycan is visible in the apo structures [42]. In the presence of Cn2, nine sugar residues were resolved (Figure 2B). The two main glycan branches embrace the Cn2 through polar interactions, burying an interface area of 520 $Å^2$ that accounts for 42% of the interface between the channel and the toxin (Figure 2C, *left*). Molecular dynamics (MD) simulations analysis confirms that the glycan lowers the binding free energy relative to a glycan-deleted variant, thereby stabilizing the complex (Figure S3B).

Cn2 engages in extensive and specific contacts with ECL_{III} and VSD_{II} (Figure 2C, *middle and right*). The α1 helix of Cn2 forms four salt bridges involving Glu1368, Arg1426, Lys1427, and Asp1436 on ECL_{III} (Figure 2C, *middle*). On the other side, the C-terminus of the globular Cn2 projects into the extracellular pocket of VSD_{II}, but at a substantially shallower position

compared to the binding pose of the spider toxin Dc1a on Na_vPaS [44] (PDB code: 6A90, Figure 2C). Cn2 forms hydrogen bonds (H-bonds) with the backbone carbonyls on the $S3\text{-}4_{II}$ linker and engages in electrostatic interactions with negatively charged residues, Glu836 and Glu838 (Figure 2C, *right*).

Cn2 binding leaves ECL_{III} almost unchanged, except a slight tilt towards the toxin (Figure S3C). In contrast, the extracellular end of the $S3_{II}$ helix forms an additional helical turn (Leu834-Glu838), whereas the first turn (Leu840-Val842) in $S4_{II}$ in the apo structure is unwound to accommodate Cn2 (Figure 2D). Glu15 of Cn2 is positioned above the gating charge residue Arg844 of $S4_{II}$. MD simulations supported persistent Glu15-Arg844 interactions, which were completely abolished when Glu15 was replaced by Arg (Figure S3D). In the presence of Cn2, $S4_{II}$ moves up by 2 Å, and the intracellular gate expands as a result of a tilt in $S6_{III}$ (Figures 2C, D and S3E).

The structural observation is supported by our mutational analysis (Figures 2E and S4, Tables S1-S2). Substitution of the VSD_{II} residue Asp836 with Lys had little effect on affinity, while the elimination of N1372-glycan by N1372A abolished detectable currents. Single point mutations to ECL_{III} residues had different impacts. Whereas E1368K also had little effect on Cn2 affinity, K1427E and D1436K both decreased channel sensitivity to Cn2, shifting the IC_{50} from 27.07 ± 3.15 nM to 158.1 ± 14.9 nM and to 1.22 ± 0.12 μM, respectively. In addition, the dose-dependent $V_{1/2}$ curves both shifted rightward, indicating reduced sensitivity to Cn2 in voltage-dependent activation.

Elongated ι-RXIA spans VSD_I and VSD_{IV} of $Na_v1.6$

In contrast to the compact structure of Cn2, ι-RXIA, whose 46 residues were also all well resolved, adopts a horizontally extended conformation and spans across VSD_I and VSD_{IV} (Figures 3A and S5A). This elongated pose of ι-RXIA, which differs markedly from the free-state NMR structures (PDB code: 2JRY) despite the presence of the four disulfide bonds [38], enables the toxin to engage in interactions with four domains in $Na_v1.6$, the C- and N-termini anchored by VSD_I and VSD_{IV}, respectively, and the middle bulk wrapping ECL_I and PD_{II}, (Figures 3A-C and S5B). We refer to this composite site as V1-4EP.

The ι-RXIA and $Na_v1.6$ interface is dominated by polar interactions. The carboxylate of Ile46 directly binds Ser217 and Arg220 on $S4_I$ (Figure 3C, *left*). The core of ι-RXIA interacts extensively with Lys907 on ECL_{II}, Ala948 and Gln950 on $S6_{II}$, and Arg344 and Glu294 on ECL_I (Figure 3C, *middle*). The amine of Gly1 is stabilized by the backbone carbonyls of Asp1544 and Gln1546 on the $S1\text{-}2_{IV}$ loop (Figure 3C, *right*). Of note, both specific and non-specific interactions with lipids are observed. Two hydrophobic residues on the outer surface of the toxin, Ile34 and Leu35, project downward to likely engage in membrane anchoring (Figure S5C).

In a sense, ι-RXIA acts as a "molecular rope" that tethers multiple domains and draws VSD_I and ECL_I towards the static core around the PD_{II} (Figure 3D). Binding of ι-RXIA results in an upward displacement of $S4_I$ relative to the apo-structure, affording a potential explanation for its agonistic effect.

To dissect the role of the specific interactions in toxin activity, we introduced nine point mutations to $Na_v1.6$, R220E, R278A, E294K, K309E, N326A, R344E, Y348A, A948Q, and Q950A, to interfere with the toxin-binding interface (Figure 3E). Except R220E, all mutants retained activities similar to the wild-type (WT) channel (Figures. S5-S6). Exposure to 1 μM ι-RXIA shifted the WT voltage-dependent activation curve by -16.5 mV ($\Delta V_{1/2}$). Four mutants (R278A, K309E, N326A, and Y348A) showed marginal changes in $\Delta V_{1/2}$, whereas the other five mutants, R220E, E294K, R344E, A948Q, and Q950A, significantly reduce the $\Delta V_{1/2}$ ($p < 0.0001$), indicating reduced agonistic effects by the toxin on these mutant channels (Figures 3E and S6). We also observed a modest increase in the inactivation time constant (τ) upon ι-RXIA treatment, which was attenuated in the R344E, A948Q, and Q950A mutants (Figure S5F and Table S3).

These findings suggest that ι-RXIA may modulate activation and inactivation through different domains. While inactivation is moderately affected through toxin interactions with the pore domain, particularly Ala948 and Gln950 on $S6_{II}$, activation concerns interactions involving the VSDs, particularly Arg220 on $S4_I$. Mutating the gating charge residue R220E led to a hyperpolarized shift in activation ($V_{1/2}$ = -38.92 ± 0.27 mV), approximating the effect of 1 μM ι-RXIA on WT channels ($V_{1/2}$ = -38.71 ± 0.33 mV) (Figure S7A and Table S3). Applying ι-RXIA to the R220E mutant caused further hyperpolarized shifts in peak current position, but with a suppressed amplitude (Figure S7A). These results suggest that electrostatic neutralization of Arg220 by the Ile46 carboxylate may account for the similar $V_{1/2}$ shifts produced by either toxin binding or the R220E mutation.

MD simulations support the above analyses (Figure S7B). Using a homology model, we constructed a "down" state model of $Na_v1.6$-VSD_I based on the experimental structure of $Na_v1.7$-M11 (PDB code: 7XVE) [45]. During triplicate 100-ns simulations, WT-$Na_v1.6$ (VSD_I up) and WT-ι-RXIA maintained stable interactions at $S4_I$, particularly between Arg220-Ile46, Ser217-Phe*44, and Ser217-Ile46 (Figure S7B). Truncation of the C-terminal residues of ι-RXIA (Δ46 or Δ45-46) or R220E of $Na_v1.6$ abolished these interactions (Figure S7). Importantly, these interactions were disrupted in the down VSD_I $Na_v1.6$, supporting our above analysis that ι-RXIA stabilizes the activated state of VSD_I (Figure S7).

Unlike the natural D-Phe*44 enantiomer, the L-Phe44 ι-RXIA only formed unstable transient contacts in the MD simulations, corresponding to increased flexibility with higher local root-mean-square fluctuation (RMSF) (Figure S7). This observation explains the higher potency of the D-Phe*44 toxin. The disparity likely reflects the extra energetic cost of correctly orienting the carboxyl group in the L-enantiomer due to stereochemical constraints.

Pc1a binds between VSD_{II} and PD_{III}

Whereas Cn2 and ι-RXIA both bind the extracellular region of the channel, the cryo-EM density reveals a single transmembrane helix corresponding to Pc1a. All 25 residues of Pc1a are resolved. The toxin wedges between $S4_{II}$ and $S6_{III}$, a site we refer to as site V2P. Pc1a binding induces a marked local rearrangement in VSD_{II}, in which the S3 and S4 hairpin tilts towards the domain interior, meanwhile pushing the intracellular half of $S2_{II}$ and $S0_{II}$ away (Figures 1F, 4A,B and S8A,B). The structure of the bound Pc1a also diverges from the helix-

turn-helix structure of free toxin (PDB code: 1G92) [46] determined by NMR (Figure S8C).

The bound Pc1a helix comprises a hydrophobic N-terminal region and a charged C-terminal end. The eight C-terminal residues, either polar or charged, specifically interact with ECL_{III}, more specifically, the $L6_{III}$ loop that links $P2_{III}$ and $S6_{III}$, via polar interactions (Figure 4C). With the Pc1a helix wedged between VSD_{II} and PD_{III}, it shares with Cn2 a common target residue, Lys1427 on $L6_{III}$ (Figures 2E and 4C). The bulk of the Pc1a helix leans against the transmembrane region of $S4_{II}$, $S5_{III}$, and $S6_{III}$ via hydrophobic interactions (Figure 4D), and the N-terminus is placed next to the S4-5_{II} linker helix, with Pro3 in proximity to Gly869 (Figure 4E).

The structural observation was validated by functional characterization of interface mutants, K1427E and G869N (Figures 4F, S8 and S9). K1427E was designed to disrupt the association with Pc1a-Asp22 on the extracellular end, and G869N was meant to increase steric hindrance to expel the N-terminus of Pc1a away from S4-5_{II}. Both mutations evidently attenuated the agonistic effect of Pc1a applied at concentrations of 10 and 30 nM (Figures 4F and S8D).

Aside from its agonistic effect through impairing fast inactivation, Pc1a substantially slows down channel activation despite a lowered voltage-dependent activation threshold (Figure S8F). The raw traces are reminiscent of the macroscopic currents of the $Na_v1.4$-WCW mutant [47]. $Na_v1.6$ exposed to 1 μM Pc1a has an even longer activation time constant (τ) at a V_{step} to -20

mV than $Na_v1.4$-WCW (Figures S1C, S8F and S9). This can be explained by its multiple contacts with $S4_{II}$, $S4\text{-}5_{II}$, $S5_{III}$ and $S6_{III}$, whose conformational changes are all directly coupled to the voltage-dependent channel activation [45,48]. With its two termini anchored by $L6_{III}$ and $S4\text{-}5_{II}$, Pc1a may hinder the movements of VSD_{II} and the ensuing $S4\text{-}5_{II}$ in response to depolarization, thereby impeding the coupling between voltage sensing and pore opening. Supporting this, G869N, a mutation to weaken the interaction between Pc1a and $S4\text{-}5_{II}$, partially rescues the activation delay caused by Pc1a (Figure S8F).

MOAs of the agonistic toxins

The structural insights provide a framework for elucidating the MOAs of the agonistic toxins. The structure of $Na_v1.6$-Cn2 supports and refines the previously proposed voltage sensor-trapping model derived from functional characterizations of β-scorpion toxins [49]. Cn2 has similar EC_{50} and IC_{50} values, suggesting that the pre-pulse barely changes toxin binding but alters voltage-dependent activation. The inhibitory effects of Cn2 may result from impeded motion of VSD_{II} if the toxin already binds to the domain in its down state. Upon pre-pulse depolarization, VSD_{II} moves upward, and the activated VSD up state is also stabilized by Cn2. The interaction between Cn2-Glu15 and Arg844 on the up $S4_{II}$ likely contributes to $S4_{II}$ trapping and the hyperpolarizing shift of the activation threshold, explaining the agonistic effect of Cn2 after pre-pulse depolarization. Supporting this, the E15R mutation has been reported to uncouple the excitatory and inhibitory activities of Cn2 [50].

Despite completely different binding pose, ι-RXIA appears to share a common effect on

the intracellular gate of $Na_v1.6$ with Cn2. Of particular note, both Cn2 and ι-RXIA place negative charges above the GC residue R2 on the corresponding S4 segment, inducing an outward displacement in the adjacent S4 helix (Figures 2D and 3E) and similar rearrangements around the $S4\text{-}5_{III}$ and $S6_{III}$, hence resulting in a dilated intracellular gate (Figure 5A-D). In both complexes, the intracellular portion of the $S6_{III}$ helix undergoes a substantial shift. The last helical turn and the subsequent residues (Lys1472-Gln1477), which are well resolved in the apo-structure, become unresolvable (Figure 5A, B). In $Na_v1.6$-Cn2, the diameter of the intracellular gate dilates to ~7 Å, similar to that in the $Na_v1.5$-QQQ mutant that disrupts fast inactivation [51] (Figure 5C, D). A marked change occurs to the densities that penetrate the gate. The linear GDN-like density in apo-$Na_v1.6$ is replaced by a branched one in both toxin-bound structures (Figure 5E). The branched density may represent a phospholipid, although other possibilities remain open. Regardless of its exact identity, accommodation of the larger molecule is consistent with a dilated gate.

By contrast, Pc1a leaves the intracellular gate essentially unchanged, where the gate-penetrating density is still GDN-like (Figure S8G). This is consistent with its minimal effect on peak current, despite its strong hyperpolarizing shift in activation. Note that Pc1a in the present $Na_v1.6$-Pc1a stabilizes the activated conformation of VSD_{II} and $S4\text{-}5_{II}$, thus offering a mechanistic explanation for the lowered threshold of activation voltage. This paradigm is shared by the three agonistic toxins, despite their completely distinct binding poses.

Discussion

$Na_v1.6$ is a key target for the development of subtype-selective antiepileptic seizure medications (ASMs) [52-56]. In this study, we have discovered three remarkably different binding sites for agonistic toxins on $Na_v1.6$, including V2EP for Cn2, V1-4EP for ι-RXIA, and V2P for Pc1a (Figure 6A). None of these binding poses has been correctly predicted by AlphaFold3 (Figure S10) [57]. These structures have expanded the structural atlas of peptide toxin binding sites not only across Na_v channels, but also for the voltage-gated ion channel superfamily (Figure 6) [2]. Of note, there is no reported peptide toxin binding site on VSD_{III} up to date, potentially due to steric occlusion by the β1 subunit (Figure 6B).

Despite adopting distinct binding poses, all three agonistic toxins forge extensive bridges between the VSD and PD, a characteristic that distinguishes them from most of the antagonistic toxins (Figure 6B). The allosteric changes and spatial constrictions observed in our structures may be critical to modulating both the channel's dynamics and kinetics, although additional conformational snapshots will be needed to confirm this link.

Beyond protein-toxin interactions, our study highlights the roles of glycans in toxin binding. The otherwise flexible N1372-glycan is stabilized by Cn2, akin to folding upon binding of some proteins (Figure 2B). Glycans on the extracellular loops have been observed to participate in toxin binding, as seen in the structure of LqhαIT bound Na_vPaS (PDB code: 8VQC). However, the interfaces are much smaller, and the glycan linked to the position equivalent to $Na_v1.6$-Asn326 is pre-stabilized by Na_v α-subunit and has little conformational

change upon toxin binding [31,58]. The $Na_v1.6$-Cn2 structure not only reveals the role of a bulky glycan as a co-receptor, but also sheds light on the design of binders that target glycans, which remain poorly characterized compared to proteins.

In sum, this work advances our understanding of how $Na_v1.6$ is modulated by agonistic peptide toxins, revealing previously uncharacterized binding poses and MOAs. These insights will facilitate rational development of targeted therapeutics using combinatorial or synergistic strategies. For instance, approaches like antibody-drug conjugates (ADCs) might be expanded by exploiting Na_v-specific recognition with other biologics (XDCs). The observed diversity in binding modes may enhance the potential for increased specificity by linking engineered toxins with small molecules.

Reference

1 Arbuckle, K. Evolutionary context of venom in animals. *Evolution of venomous animals and their toxins* **24**, 3-31 (2017).

2 Huang, J., Pan, X. & Yan, N. Structural biology and molecular pharmacology of voltage-gated ion channels. *Nature Reviews Molecular Cell Biology*, 1-22 (2024).

3 Deuis, J. R., Mueller, A., Israel, M. R. & Vetter, I. The pharmacology of voltage-gated sodium channel activators. *Neuropharmacology* **127**, 87-108 (2017).

4 de Lera Ruiz, M. & Kraus, R. L. Voltage-gated sodium channels: structure, function, pharmacology, and clinical indications. *Journal of medicinal chemistry* **58**, 7093-7118 (2015).

5 Lazarovici, P. Snake-and spider-venom-derived toxins as lead compounds for drug development. *Snake and Spider Toxins: Methods and Protocols*, 3-26 (2020).

6 Kalia, J. *et al.* From foe to friend: using animal toxins to investigate ion channel function. *Journal of molecular biology* **427**, 158-175 (2015).

7 Luz Morales-Lazaro, S., Hernández-García, E., Serrano-Flores, B. & Rosenbaum, T. Organic toxins as tools to understand ion channel mechanisms and structure. *Current Topics in Medicinal Chemistry* **15**, 581-603 (2015).

8 Escoubas, P. & Bosmans, F. Spider peptide toxins as leads for drug development. *Expert opinion on drug discovery* **2**, 823-835 (2007).

9 Terlau, H. & Olivera, B. M. Conus venoms: a rich source of novel ion channel-targeted peptides. *Physiol Rev* **84**, 41-68 (2004). https://doi.org:10.1152/physrev.00020.2003

10 Zipes, D. P. & Jalife, J. *Cardiac electrophysiology: from cell to bedside, chapter 1*. (Saunders, 2021).

11 Fan, X. *et al.* Phrixotoxin-3 binds to three distinct antagonistic sites on human Nav1.6. *Cell Research* **In revision** (2025).

12 Schaller, K. L., Krzemien, D. M., Yarowsky, P. J., Krueger, B. K. & Caldwell, J. H. A novel, abundant sodium channel expressed in neurons and glia. *J Neurosci* **15**, 3231-3242 (1995). https://doi.org:10.1523/JNEUROSCI.15-05-03231.1995

13 Freeman, S. A., Desmazières, A., Fricker, D., Lubetzki, C. & Sol-Foulon, N. Mechanisms of sodium channel clustering and its influence on axonal impulse conduction. *Cellular and Molecular Life Sciences* **73**, 723-735 (2016).

14 Caldwell, J. H., Schaller, K. L., Lasher, R. S., Peles, E. & Levinson, S. R. Sodium channel Nav1. 6 is localized at nodes of Ranvier, dendrites, and synapses. *Proceedings of the National Academy of Sciences* **97**, 5616-5620 (2000).

15 Lorincz, A. & Nusser, Z. Cell-type-dependent molecular composition of the axon initial segment. *J Neurosci* **28**, 14329-14340 (2008). https://doi.org:10.1523/JNEUROSCI.4833-08.2008

16 Hu, W. *et al.* Distinct contributions of Na(v)1.6 and Na(v)1.2 in action potential initiation and backpropagation. *Nat Neurosci* **12**, 996-1002 (2009). https://doi.org:10.1038/nn.2359

17 O'Brien, J. E. & Meisler, M. H. Sodium channel SCN8A (Nav1.6): properties and de novo mutations in epileptic encephalopathy and intellectual disability. *Front Genet* **4**, 213 (2013). https://doi.org:10.3389/fgene.2013.00213

18 Liu, Y. *et al.* Neuronal mechanisms of mutations in SCN8A causing epilepsy or intellectual disability. *Brain* **142**, 376-390 (2019).

19 Blanchard, M. G. *et al.* De novo gain-of-function and loss-of-function mutations of SCN8A in patients with intellectual disabilities and epilepsy. *Journal of medical genetics* **52**, 330-337 (2015).

20 Sole, L., Wagnon, J. L. & Tamkun, M. M. Functional analysis of three Na(v)1.6 mutations causing early

infantile epileptic encephalopathy. *Biochim Biophys Acta Mol Basis Dis* **1866**, 165959 (2020). https://doi.org:10.1016/j.bbadis.2020.165959

21 Tanaka, B. S. *et al.* A gain-of-function mutation in Nav1. 6 in a case of trigeminal neuralgia. *Molecular medicine* **22**, 338-348 (2016).

22 Wagnon, J. L. *et al.* Loss-of-function variants of SCN8A in intellectual disability without seizures. *Neurology: Genetics* **3**, e170 (2017).

23 Wagnon, J. L. *et al.* Partial loss-of-function of sodium channel SCN8A in familial isolated myoclonus. *Human mutation* **39**, 965-969 (2018).

24 Pan, X. *et al.* Molecular basis for pore blockade of human Na+ channel Nav1. 2 by the μ-conotoxin KIIIA. *Science* **363**, 1309-1313 (2019).

25 Shen, H., Liu, D., Wu, K., Lei, J. & Yan, N. Structures of human Na(v)1.7 channel in complex with auxiliary subunits and animal toxins. *Science* **363**, 1303-1308 (2019). https://doi.org:10.1126/science.aaw2493

26 Huang, G. *et al.* High-resolution structures of human Na(v)1.7 reveal gating modulation through alpha-pi helical transition of S6(IV). *Cell Rep* **39**, 110735 (2022). https://doi.org:10.1016/j.celrep.2022.110735

27 Li, Y. *et al.* Structure of human NaV1. 6 channel reveals Na+ selectivity and pore blockade by 4, 9-anhydro-tetrodotoxin. *Nature Communications* **14**, 1030 (2023).

28 Li, Z. *et al.* Structural basis for pore blockade of the human cardiac sodium channel Nav1. 5 by tetrodotoxin and quinidine. *biorxiv*, 2019.2012. 2030.890681 (2019).

29 Jalife, J. & Stevenson, W. G. *Zipes and Jalife's Cardiac Electrophysiology: From Cell to Bedside, E-Book*. (Elsevier Health Sciences, 2021).

30 Shen, H. *et al.* Structural basis for the modulation of voltage-gated sodium channels by animal toxins. *Science* **362**, eaau2596 (2018).

31 Clairfeuille, T. *et al.* Structural basis of α-scorpion toxin action on Nav channels. *Science* **363**, eaav8573 (2019).

32 Jiang, D. *et al.* Structural basis for voltage-sensor trapping of the cardiac sodium channel by a deathstalker scorpion toxin. *Nature Communications* **12**, 128 (2021).

33 Bosmans, F. *et al.* Four novel tarantula toxins as selective modulators of voltage-gated sodium channel subtypes. *Molecular pharmacology* **69**, 419-429 (2006).

34 Fiedler, B. *et al.* Specificity, affinity and efficacy of iota-conotoxin RXIA, an agonist of voltage-gated sodium channels Na(V)1.2, 1.6 and 1.7. *Biochem Pharmacol* **75**, 2334-2344 (2008). https://doi.org:10.1016/j.bcp.2008.03.019

35 Jimenez, E. C. *et al.* Novel excitatory Conus peptides define a new conotoxin superfamily. *J Neurochem* **85**, 610-621 (2003). https://doi.org:10.1046/j.1471-4159.2003.01685.x

36 Schiavon, E. *et al.* Resurgent current and voltage sensor trapping enhanced activation by a beta-scorpion toxin solely in Nav1.6 channel. Significance in mice Purkinje neurons. *J Biol Chem* **281**, 20326-20337 (2006). https://doi.org:10.1074/jbc.M600565200

37 Aili, S. R. *et al.* An integrated proteomic and transcriptomic analysis reveals the venom complexity of the bullet ant Paraponera clavata. *Toxins* **12**, 324 (2020).

38 Buczek, O. *et al.* Structure and sodium channel activity of an excitatory I1-superfamily conotoxin. *Biochemistry* **46**, 9929-9940 (2007). https://doi.org:10.1021/bi700797f

39 Buczek, O., Yoshikami, D., Bulaj, G., Jimenez, E. C. & Olivera, B. M. Post-translational amino acid isomerization: a functionally important D-amino acid in an excitatory peptide. *J Biol Chem* **280**, 4247-4253 (2005). https://doi.org:10.1074/jbc.M405835200

40 Piek, T. *et al.* Poneratoxin, a novel peptide neurotoxin from the venom of the ant, Paraponera clavata. *Comparative Biochemistry and Physiology Part C: Comparative Pharmacology* **99**, 487-495 (1991).

41 Robinson, S. D. *et al.* Ant venoms contain vertebrate-selective pain-causing sodium channel toxins. *Nature Communications* **14**, 2977 (2023).

42 Fan, X., Huang, J., Jin, X. & Yan, N. Cryo-EM structure of human voltage-gated sodium channel Na(v)1.6. *Proc Natl Acad Sci U S A* **120**, e2220578120 (2023). https://doi.org:10.1073/pnas.2220578120

43 Wu, Q. *et al.* Structural mapping of Na(v)1.7 antagonists. *Nat Commun* **14**, 3224 (2023). https://doi.org:10.1038/s41467-023-38942-3

44 Shen, H. *et al.* Structural basis for the modulation of voltage-gated sodium channels by animal toxins. *Science (New York, N.Y* **362** (2018). https://doi.org:10.1126/science.aau2596

45 Huang, G. *et al.* Unwinding and spiral sliding of S4 and domain rotation of VSD during the electromechanical coupling in Na(v)1.7. *Proc Natl Acad Sci U S A* **119**, e2209164119 (2022). https://doi.org:10.1073/pnas.2209164119

46 Szolajska, E. *et al.* Poneratoxin, a neurotoxin from ant venom: Structure and expression in insect cells and construction of a bio-insecticide. *European journal of biochemistry* **271**, 2127-2136 (2004).

47 Goldschen-Ohm, M. P., Capes, D. L., Oelstrom, K. M. & Chanda, B. Multiple pore conformations driven by asynchronous movements of voltage sensors in a eukaryotic sodium channel. *Nature communications* **4**, 1350 (2013).

48 Gao, S. *et al.* Structural basis for human Cav1. 2 inhibition by multiple drugs and the neurotoxin calciseptine. *Cell* **186**, 5363-5374. e5316 (2023).

49 Cestèle, S. *et al.* Voltage sensor–trapping: enhanced activation of sodium channels by β-scorpion toxin bound to the S3–S4 loop in domain II. *Neuron* **21**, 919-931 (1998).

50 Israel, M. R. *et al.* The E15R point mutation in scorpion toxin Cn2 uncouples its depressant and excitatory activities on human NaV1. 6. *Journal of medicinal chemistry* **61**, 1730-1736 (2018).

51 Jiang, D. *et al.* Open-state structure and pore gating mechanism of the cardiac sodium channel. *Cell* **184**, 5151-5162 e5111 (2021). https://doi.org:10.1016/j.cell.2021.08.021

52 Wisedchaisri, G. & Gamal El-Din, T. M. Druggability of Voltage-Gated Sodium Channels-Exploring Old and New Drug Receptor Sites. *Front Pharmacol* **13**, 858348 (2022). https://doi.org:10.3389/fphar.2022.858348

53 Fattorusso, A. *et al.* The Pharmacoresistant Epilepsy: An Overview on Existant and New Emerging Therapies. *Front Neurol* **12**, 674483 (2021). https://doi.org:10.3389/fneur.2021.674483

54 Stevens, M., Peigneur, S. & Tytgat, J. Neurotoxins and their binding areas on voltage-gated sodium channels. *Front Pharmacol* **2**, 71 (2011). https://doi.org:10.3389/fphar.2011.00071

55 Bagal, S. K., Marron, B. E., Owen, R. M., Storer, R. I. & Swain, N. A. Voltage gated sodium channels as drug discovery targets. *Channels (Austin)* **9**, 360-366 (2015). https://doi.org:10.1080/19336950.2015.1079674

56 Blumenfeld, H. *et al.* Role of hippocampal sodium channel Nav1. 6 in kindling epileptogenesis. *Epilepsia* **50**, 44-55 (2009).

57 Abramson, J. *et al.* Accurate structure prediction of biomolecular interactions with AlphaFold 3. *Nature* **630**, 493-500 (2024).

58 Phulera, S. *et al.* Scorpion alpha-toxin LqhalphaIT specifically interacts with a glycan at the pore domain of voltage-gated sodium channels. *Structure* (2024). https://doi.org:10.1016/j.str.2024.07.021

59 Punjani, A., Rubinstein, J. L., Fleet, D. J. & Brubaker, M. A. cryoSPARC: algorithms for rapid unsupervised cryo-EM structure determination. *Nat Methods* **14**, 290-296 (2017).

https://doi.org:10.1038/nmeth.4169

60 Lei, J. & Frank, J. Automated acquisition of cryo-electron micrographs for single particle reconstruction on an FEI Tecnai electron microscope. *Journal of structural biology* **150**, 69-80 (2005).

61 Bepler, T. *et al.* Positive-unlabeled convolutional neural networks for particle picking in cryo-electron micrographs. *Nature methods* **16**, 1153-1160 (2019).

62 Emsley, P., Lohkamp, B., Scott, W. G. & Cowtan, K. Features and development of Coot. *Acta Crystallogr D Biol Crystallogr* **66**, 486-501 (2010). https://doi.org:10.1107/S0907444910007493

63 Pintar, A., Possani, L. D. & Delepierre, M. Solution structure of toxin 2 from Centruroides noxius Hoffmann, a β-scorpion neurotoxin acting on sodium channels. *Journal of molecular biology* **287**, 359-367 (1999).

64 Afonine, P. V. *et al.* Towards automated crystallographic structure refinement with phenix.refine. *Acta Crystallogr D Biol Crystallogr* **68**, 352-367 (2012). https://doi.org:10.1107/S0907444912001308

65 Croll, T. I. ISOLDE: a physically realistic environment for model building into low-resolution electron-density maps. *Acta Crystallogr D Struct Biol* **74**, 519-530 (2018). https://doi.org:10.1107/S2059798318002425

66 Li, Z. *et al.* Structure of human Na(v)1.5 reveals the fast inactivation-related segments as a mutational hotspot for the long QT syndrome. *Proc Natl Acad Sci U S A* **118** (2021). https://doi.org:10.1073/pnas.2100069118

67 Huang, X. *et al.* Structural basis for high-voltage activation and subtype-specific inhibition of human Na(v)1.8. *Proc Natl Acad Sci U S A* **119**, e2208211119 (2022). https://doi.org:10.1073/pnas.2208211119

68 Sastry, G. M., Adzhigirey, M., Day, T., Annabhimoju, R. & Sherman, W. Protein and ligand preparation: parameters, protocols, and influence on virtual screening enrichments. *J Comput Aided Mol Des* **27**, 221-234 (2013). https://doi.org:10.1007/s10822-013-9644-8

69 Lu, C. *et al.* OPLS4: Improving Force Field Accuracy on Challenging Regimes of Chemical Space. *J Chem Theory Comput* **17**, 4291-4300 (2021). https://doi.org:10.1021/acs.jctc.1c00302

70 Lomize, A. L., Todd, S. C. & Pogozheva, I. D. Spatial arrangement of proteins in planar and curved membranes by PPM 3.0. *Protein Sci* **31**, 209-220 (2022). https://doi.org:10.1002/pro.4219

71 Mark, P. & Nilsson, L. Structure and dynamics of the TIP3P, SPC, and SPC/E water models at 298 K. *The Journal of Physical Chemistry A* **105**, 9954-9960 (2001).

72 McGibbon, R. T. *et al.* MDTraj: A Modern Open Library for the Analysis of Molecular Dynamics Trajectories. *Biophys J* **109**, 1528-1532 (2015). https://doi.org:10.1016/j.bpj.2015.08.015

73 Pérez-Hernández, G. & Hildebrand, P. W. Mdciao: accessible analysis and visualization of molecular dynamics simulation data. *BioRxiv*, 2022.2007. 2015.500163 (2022).

74 Pettersen, E. F. *et al.* UCSF ChimeraX: Structure visualization for researchers, educators, and developers. *Protein Sci* **30**, 70-82 (2021). https://doi.org:10.1002/pro.3943

75 Smart, O. S., Neduvelil, J. G., Wang, X., Wallace, B. A. & Sansom, M. S. HOLE: a program for the analysis of the pore dimensions of ion channel structural models. *J Mol Graph* **14**, 354-360, 376 (1996). https://doi.org:10.1016/s0263-7855(97)00009-x

Acknowledgements

We thank the cryo-EM facility at Princeton Imaging and Analysis Center. We thank the Structural Biology Core Facility at the Bio-Tech Center and the Computing Labware for Electron-microscopy Visualization and Experimental Research (CLEVER) at the Biomedical Data Center of Shenzhen Medical Academy of Research and Translation (SMART) for their technical support. This work is supported by the National Natural Science Foundation of China (32330052, 92478205, and 32501082). X.F. has been supported by the HFSP long-term fellowship (LT000754/2020-L) from the International Human Frontier Science Program Organization (HFSPO) from 2020 to 2023. J.H. and X.F. are supported by the start-up funding from Shenzhen Medical Academy of Research and Translation (SMART). J.H. is also supported by the Guangdong Pearl River Talent Program (ZJQNRC20241219163128017). X.J. is supported by Beijing Natural Science Foundation (7264373). N.Y. thanks the Parkland Foundation for the Mindray Endowed Professorship.

Author Contributions

N.Y., X.F., and J.H. conceived the project. X.F., J.H., L.Y., J.C., H.W., X.H., J.G., Q.W., Y.X., F.L., Q.G., Z.S., X.J., and N.Y. designed experiments; X.F., J.H. and L.Y. performed all experiments related to cryo-EM studies, including protein expression, purification and 3D reconstructions; J.C., Q.W., Q.G., X.H., Z.S., and X.J. carried out experiments related to electrophysiology; X.H., Y.X., and F.L. prepared the plasmids for electrophysiological analyses; H.W. performed molecular dynamics simulations; X.F., J.H., L.Y., J.C., H.W., X.H., J.G., Q.W., Y.X., F.L., Q.G., Z.S., X.J., and N.Y. analyzed date; X.F., J.H., and N.Y. wrote the manuscript

with input from all authors. All authors approved the final manuscript.

Competing Interest

The authors declare no competing interests.

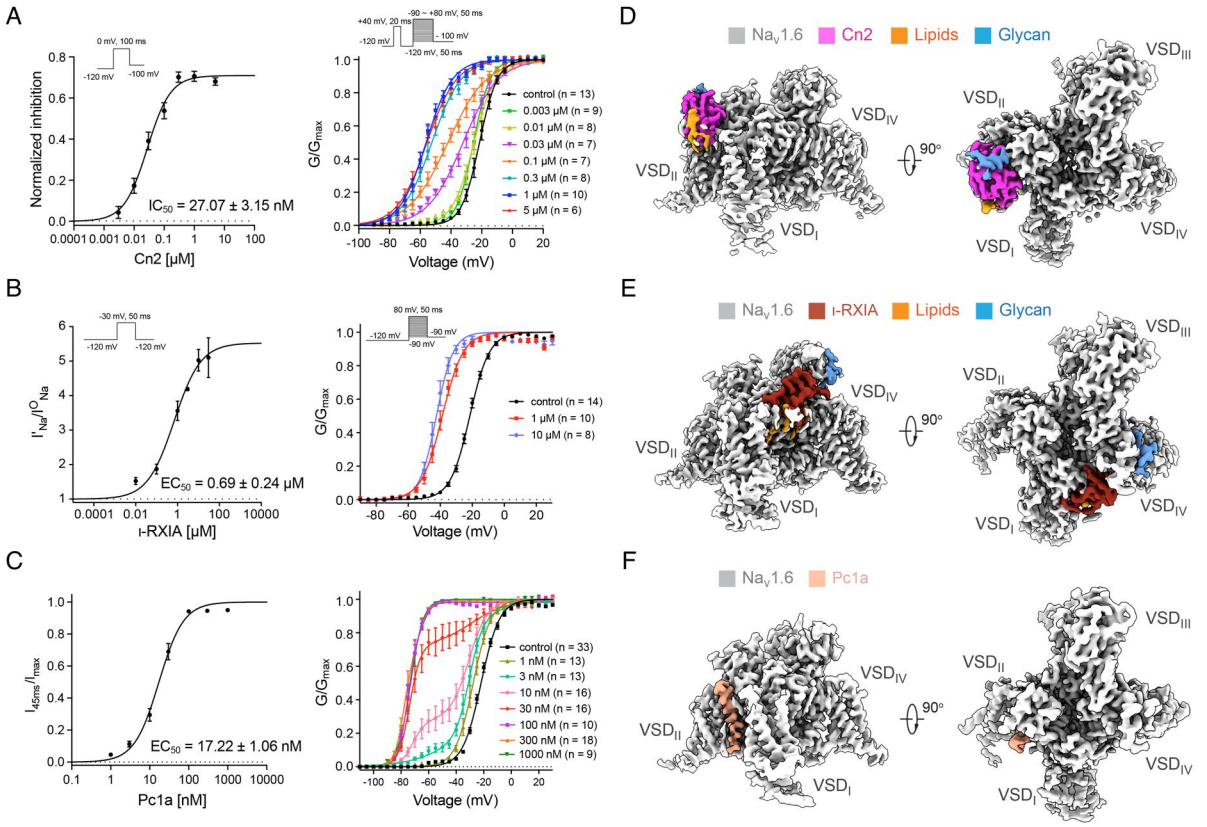

Figure 1 | Functional and structural characterizations of $Na_v1.6$ modulation by three peptide toxins. **A,** Dual modulation of $Na_v1.6$ by the β-scorpion toxin Cn2. *Left*: Cn2 inhibits $Na_v1.6$ at steady state, with the IC_{50} of 27.07 ± 3.15 nM. The sample sizes (n) for low to high concentrations are n = 10, 10, 9, 10, 10, 10, 8. Shown here is the normalized dose-dependent response curve of steady-state inhibition of $Na_v1.6$ by Cn2. Sodium currents were elicited from -120 mV, then stepped to 0 mV for 100 ms. *Right*: Cn2 acts as an agonist by lowering the activation threshold of $Na_v1.6$. Activation curves were obtained by applying a brief pre-pulse to +40 mV for 20 ms followed by -120 mV for 50 ms, then stepped to depolarizing pulses from -90 to +65 mV in 5 mV increments. **B,** Characterization of the agonistic effect of ι-conotoxin-RXIA (ι-RXIA) on human $Na_v1.6$. *Left*: The ratio of peak currents with (I'_{Na}) and without (I^o_{Na}) the peptide toxin confirms the activation of $Na_v1.6$ by ι-RXIA with EC_{50} of 0.69 ± 0.24 μM. The sample sizes (n) for low to high concentrations are n= 6, 10, 12, 3, 9, 8. Sodium currents

were elicited from -120 mV, then step to -30 mV for 50 ms. *Right*: Activation curves of $Na_v1.6$ treated with 1 μM or 10 μM ι-RXIA. Cells were held at -120 mV following a 50 ms depolarizing pulse from -90 to +80 mV in 5 mV increments. **C,** In-house synthesized ant poneratoxin Pc1a activates human $Na_v1.6$. *Left*: Pc1a potentiates $Na_v1.6$ with an EC_{50} of 17.22 ± 1.06 nM. The response was sustained current (I_{45ms})/peak current (I_{max}). The sample sizes (n) for low to high concentrations are n= 40, 29, 29, 30, 35, 27, 22, 10. Sodium currents were elicited from -120 mV, then step to -20 mV for 50 ms. *Right*: Activation curves of $Na_v1.6$ treated with increasing concentrations of Pc1a. Cells were held at -120 mV following a 500 ms depolarizing pulse from -110 to +60 mV in 5 mV increments. For panels **A-C**, data are presented as mean ± SEM, and sample sizes (n) are shown in each panel. **D-E,** Overall cryo-EM maps of $Na_v1.6$ (white) in complex with Cn2 (magenta, **D**), ι-RXIA (brown, **E**), and Pc1a (salmon, **F**) at averaged resolutions of 2.8 Å, 2.5 Å and 3.1 Å, respectively. Two perpendicular views are shown for each reconstruction. Functionally important glycans and bound lipids are colored blue and orange, respectively. All EM maps were prepared in ChimeraX [74] and contoured at 7 σ in all figures if not otherwise indicated.

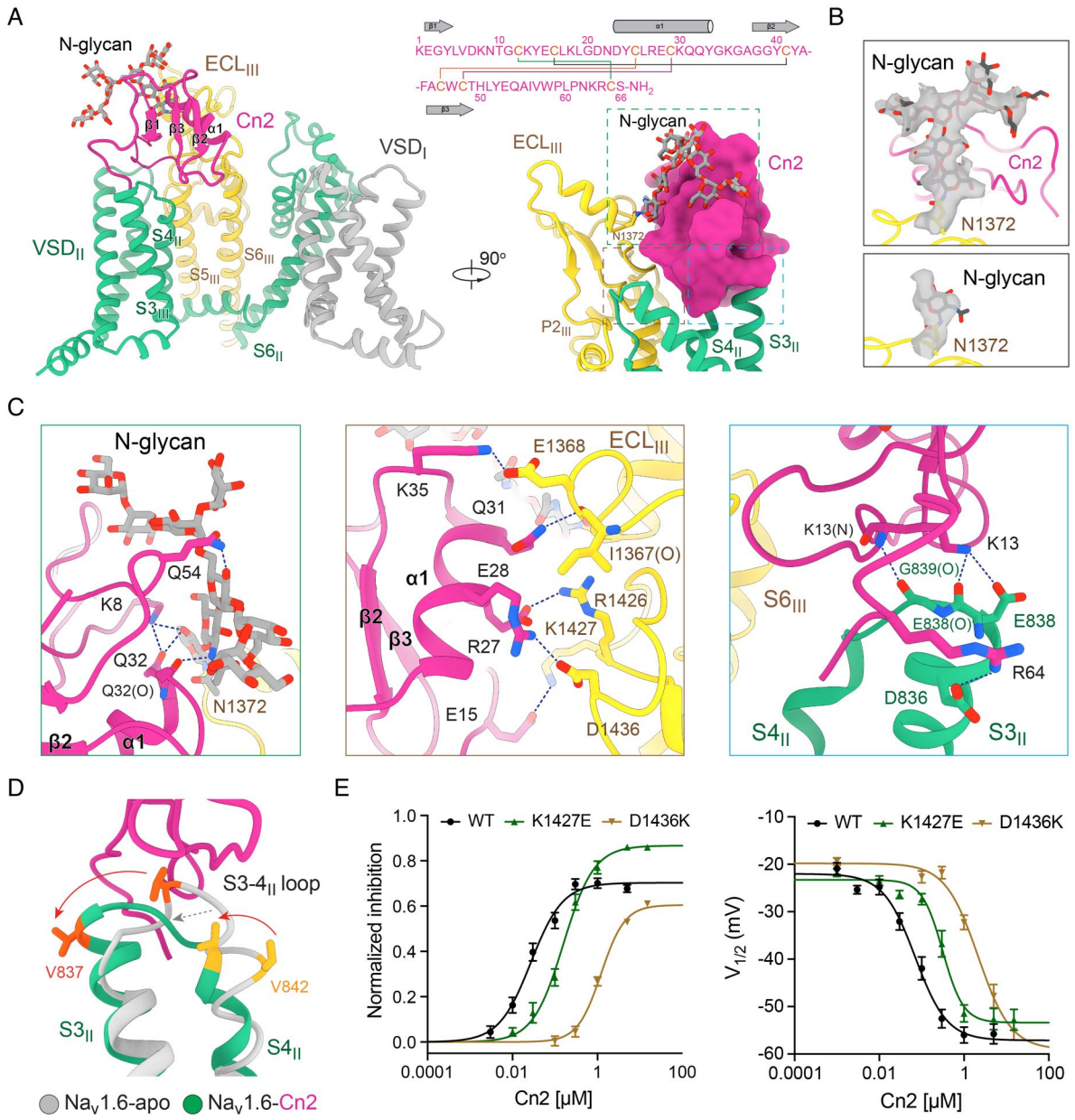

Figure 2 | A branched glycan constitutes part of the receptor site for Cn2. **A,** Cn2 is coordinated by VSD$_{II}$, ECL$_{III}$, and a branched glycan linked to Asn1372 (N1372-glycan). The primary sequence of Cn2, along with its secondary structures and four disulfide bonds, is shown above the right panel. **B,** Binding of Cn2 stabilizes N1372-glycan. While the entire Asn1372-glycan is well resolved in Cn2-bound Na$_V$1.6 (*upper*), only one sugar residue is visible in the apo channel (*lower*). **C,** Coordination of Cn2 by Na$_V$1.6 through extensive electrostatic interactions. Illustrated here are detailed interactions between Cn2 and N1372-

glycan (*left*), ECL_{III} (*middle*), and VSD_{II} (*right*). **D,** Cn2 stabilizes an up conformation of $Na_v1.6$-VSD_{II}. Structures of Cn2-bound and apo $Na_v1.6$ are superimposed relative to the overall channel. The structural shifts in $S3_{II}$, $S4_{II}$, and the $S3\text{-}4_{II}$ loop upon Cn2 binding are indicated by red arrows. **E,** Functional validation of the channel-toxin interactions. *Left:* Normalized dose-response curves for steady-state inhibition of $Na_v1.6$ variants by Cn2, including WT and two mutants K1427E and D1436K. The IC_{50} values are 27.07 ± 3.15 nM for WT, 158.1 ± 15.9 nM for K1427E ($P < 0.0001$, compared with WT), and 1219 ± 120 nM for D1436K ($P < 0.0001$, compared with WT). The sample sizes (n) for low to high concentrations are n = 10, 10, 9, 10, 10, 10, 8 for WT; n = 11, 12, 14, 15, 14, 11, 9 for K1427E; n = 14, 13, 13, 15, 10 for D1436K. *Right:* Dose-dependent curves for activation $V_{1/2}$ with a pre-pulse to + 40 mV of $Na_v1.6$ variants. The EC_{50} values are 70.40 ± 11.27 nM for WT, 314.7 ± 19.59 nM for K1427E, and 2155 ± 441 nM for D1436K. The sample sizes (n) for low to high concentrations are n = 14, 9, 8, 7, 7, 8, 10, 6 for WT; n = 19, 10, 10, 11, 11, 10, 9, 8 for K1427E; n = 19, 14, 11, 11, 12, 9 for D1436K.

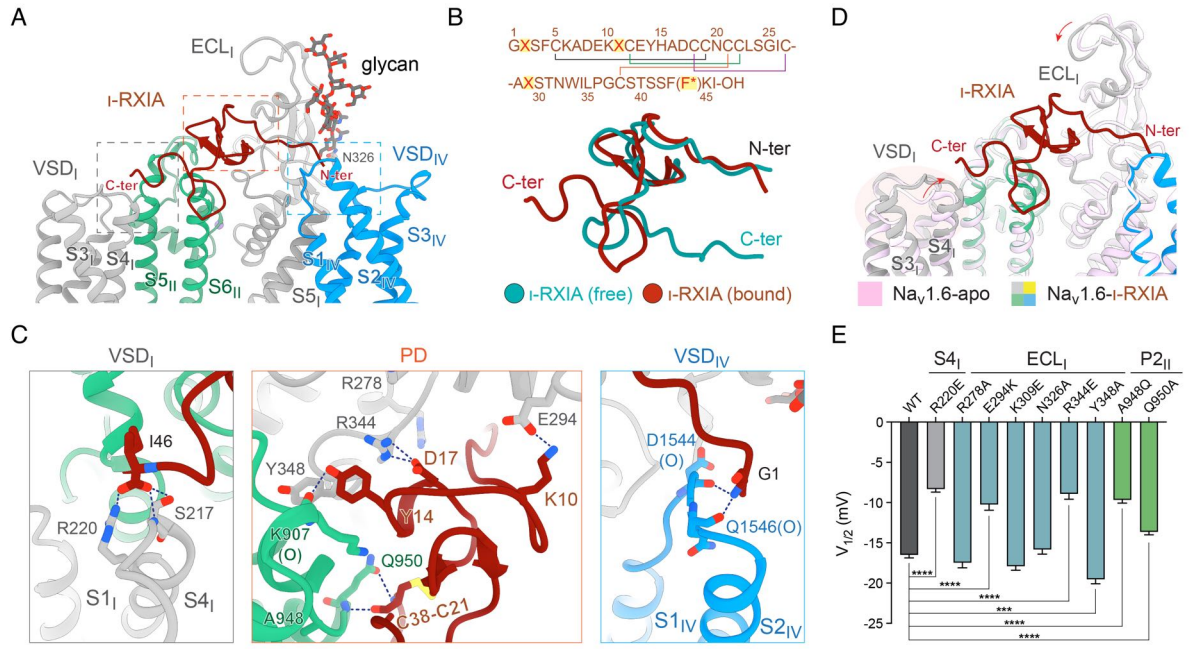

Figure 3 | The elongated structure of ι-RXIA spans the extracellular side across VSD$_I$ and VSD$_{IV}$ of Na$_v$1.6. **A,** ι-RXIA spans VSD$_I$ (grey) and VSD$_{IV}$ (blue), covering the shoulder of PD$_{II}$ (green). The amino (N) and carboxy (C) termini of ι-RXIA are anchored to the extracellular regions of VSD$_{IV}$ and VSD$_I$, respectively. **B,** Pronounced structural changes in ι-RXIA upon binding to Na$_v$1.6. The primary sequence of ι-RXIA, containing four pairs of disulfide bonds, is presented on the top. X: hydroxyproline; F*: D-phenylalanine. Shown below are the superimposed cryo-EM structures of ι-RXIA bound to Na$_v$1.6 and the NMR structure of the free toxin (PDB: 2JRY). **C,** Detailed interactions between ι-RXIA and Na$_v$1.6. Close-up views are shown for the interactions between ι-RXIA and S4$_I$ (*left*), PD$_{II}$ and ECL$_I$ (*middle*), and the S1-2$_{IV}$ loop (*right*). **D,** The C-terminus of ι-RXIA stabilizes an "up" conformation of the S4$_I$ segment. Structures of ι-RXIA-bound and apo-Na$_v$1.6 are superimposed relative to the entire channel, with structural shifts of Na$_v$1.6 upon ι-RXIA binding indicated by red arrows. **E,** Functional validation of the structure-revealed interactions. Changes in the half-maximal activation voltage ($\Delta V_{1/2}$) are presented for WT Na$_v$1.6 and structure-guided mutants in the

presence of 1 μM ι-RXIA. The sample sizes (n) for WT and mutants are n = 10, 13, 7, 9, 7, 8, 6, 7, 9.13. Error bars represent mean ± SEM.

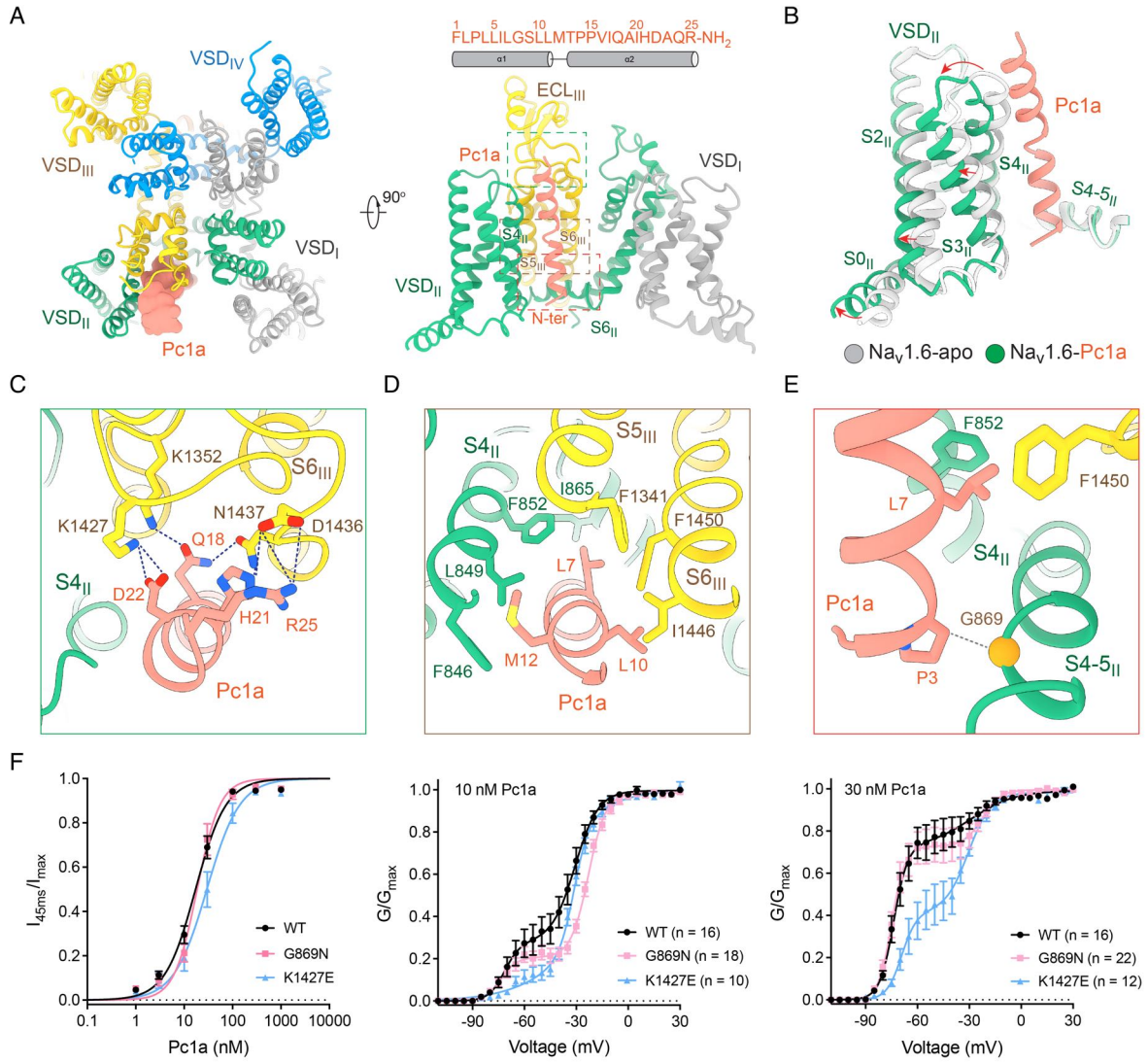

Figure 4 | Membrane-spanning Pc1a binds to $Na_v1.6$ at the VSD_{II}-PD interface. **A,** Pc1a folds to a transmembrane helix that stands between VSD_{II} and PD. The Pc1a helix, with a kink in the middle, positions its amino terminus on the intracellular side. The primary sequence of Pc1a and its secondary structures are shown above, and this binding site will be referred to as V2P. **B,** Pc1a binding induces structural shift of VSD_{II}. The structure of Pc1a-bound $Na_v1.6$ (domain colored) is superimposed to that of the apo channel (white). The structural changes of VSD_{II} upon Pc1a binding are indicated by red arrows. **C-E,** Pc1a tethers VSD_{II} with ECL_{III} on the extracellular side and $S4\text{-}5_{II}$ on the intracellular side. Extracellular views are shown in panels **C** and **D**, and a side view is presented in panel **E** Polar interactions are indicated with

blue dashed lines. **F,** Functional validation of the channel-toxin interactions. *Left:* Normalized dose-response curves for activation of $Na_v1.6$ variants by Pc1a, including WT and two mutants K1427E and G869N. Differential performance of G-V curves between $Na_v1.6$ WT and two mutants during electrophysiological recordings in the presence of 10 nM (*middle*) and 30 nM (*right*) Pc1a fitted by double Boltzmann equations. The sample sizes (n) in left panel for low to high concentrations are n =40, 29, 29, 30, 35, 27, 22, 10 for WT; n = 22, 8, 9, 13, 22, 21, 8, 12 for G869N; n =18, 10, 10, 15, 17, 18, 11 ,6 for K1427E. The sample sizes (n) in middle and right panel are n=16, 18, 10 for 10 nM and n=16, 22, 12 for 30 nM.

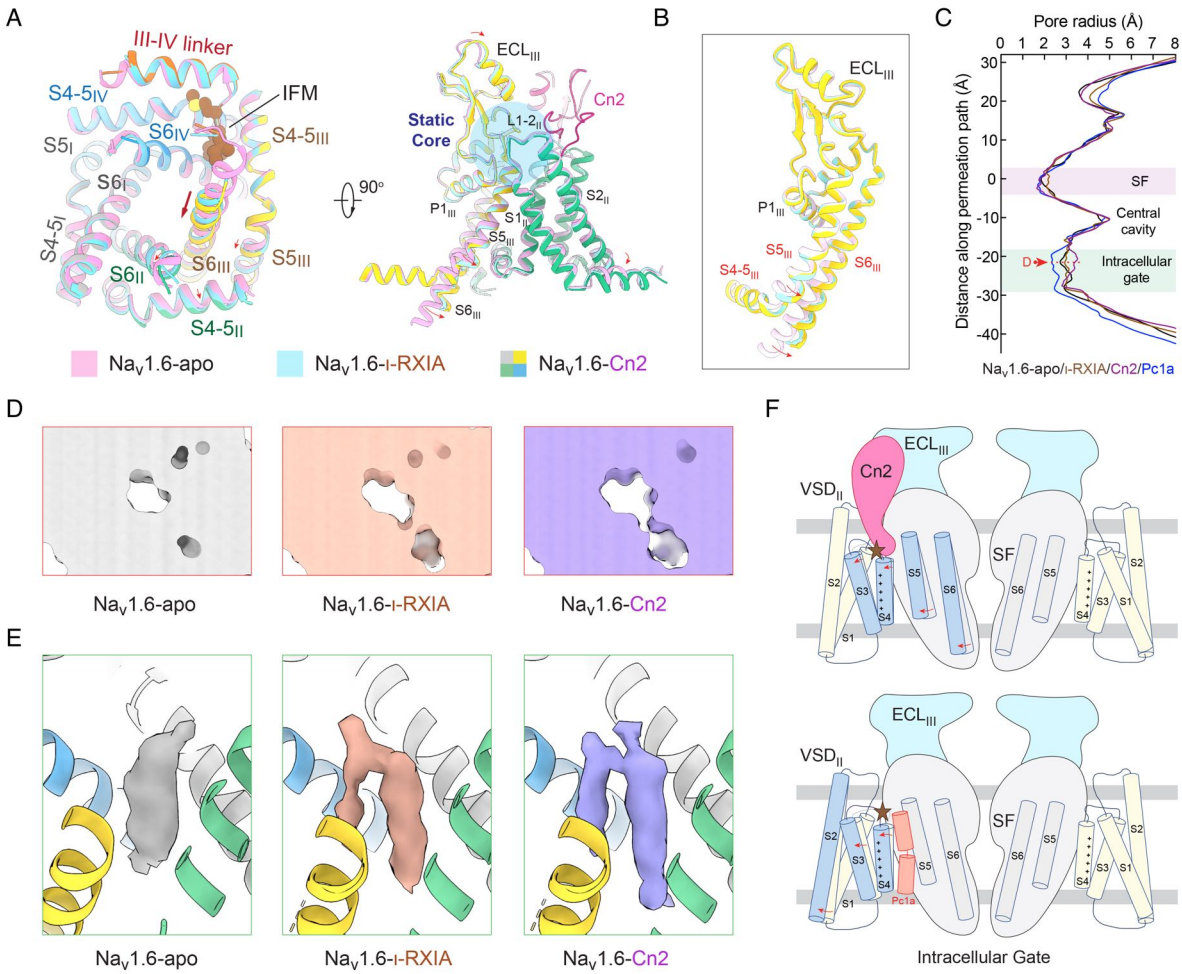

Figure 5 | Cn2 and ι-RXIA both dilate the intracellular gate. **A,** The intracellular gate of $Na_v1.6$ is dilated in the presence of ι-RXIA or Cn2. Shown here is a cytosolic view of superimposed structures of $Na_v1.6$ with ι-RXIA (light blue), Cn2 (domain colored), or without ligand (pink). **B,** Conformational shifts of PD_{III} and the adjacent VSD_{II}. The rearrangements of $S4\text{-}5_{III}$, $S5_{III}$ and $S6_{III}$ upon ι-RXIA or Cn2 binding are highlighted in the inset. **C,** Size changes of the ion-permeating path upon toxin binding. The pore radius plots along the permeation pathway of apo- and toxin-bound $Na_v1.6$ were estimated using the HOLE program [75]. "D" denotes the point where the intracellular gate dilates most in the presence of Cn2. **D,** Dilation of the intracellular gate upon binding to ι-RXIA or Cn2. Shown here is a cross-sectional view of the intracellular gate in the presence of ι-RXIA and Cn2 compared to the apo-state $Na_v1.6$.

E, The molecule occupying the intracellular gate in ι-RXIA or Cn2-bound $Na_v1.6$ is different from that in the apo channel. In ligand-free $Na_v1.6$ and all other 3D EM maps of ligand-free, WT human Na_v channels, an elongated density, reminiscent of a sterol or detergent molecules like GDN and digitonin, is always present to penetrate the intracellular gate. In ι-RXIA or Cn2-bound $Na_v1.6$, however, the density has two tails, reminiscent of a phospholipid, although the identity remains unclear. **F,** Cn2 and Pc1a both stabilize the activated conformation of VSD_{II} despite completely different binding poses. Conformational changes upon toxin binding are highlighted by red arrows.

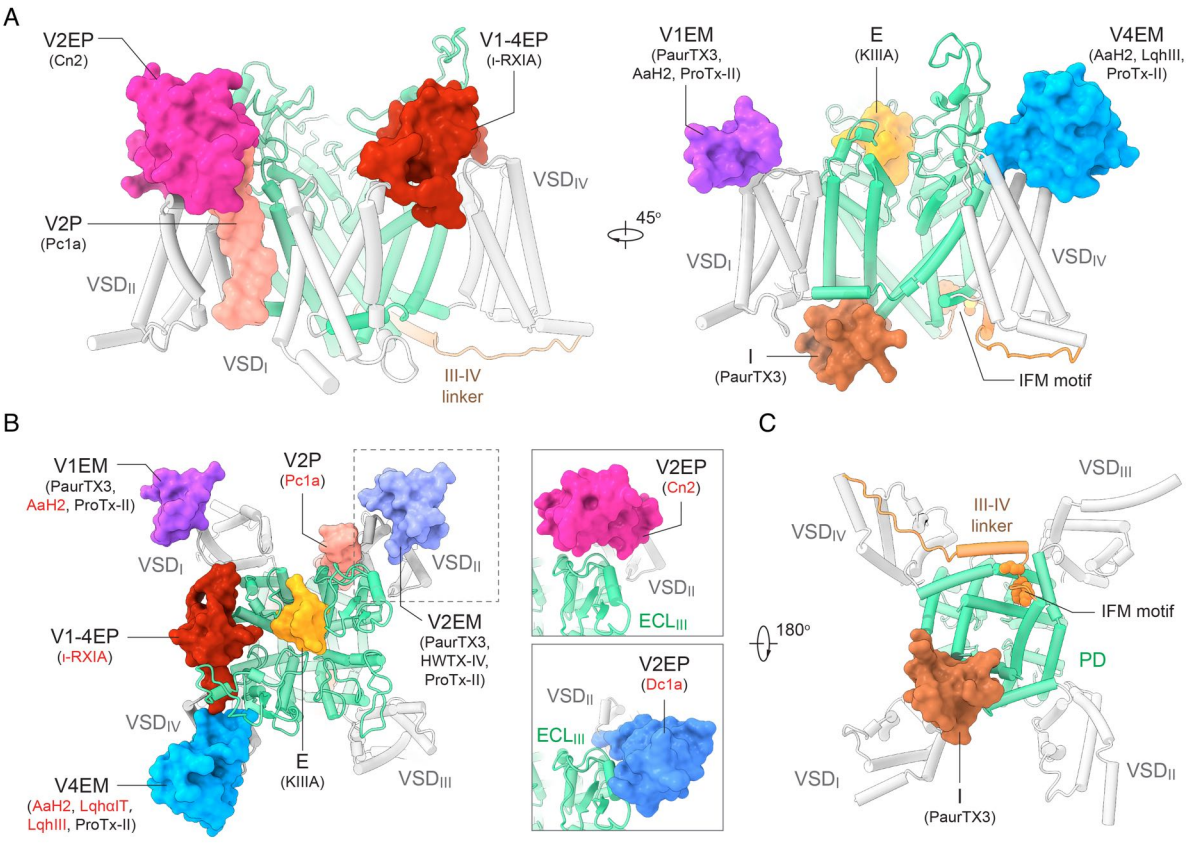

Figure 6 | Summary of peptide toxin binding sites identified on Na_v channels. Shown here are side (**A**), extracellular (**B**), and intracellular (**C**) views of the Na_v channel with diverse receptor sites for peptide modulators using a structure-based nomenclature system [43]. The four VSDs are represented by V1 to V4. E: extracellular; P: pore domain; I: inactivation motif binding site. The toxins are labeled in brackets under the corresponding binding sites. Some toxins, like AaH2 and PaurTX3, can bind to multiple sites. Agonists are labeled red.